Grid resolution assessment in wall-modeled large-eddy simulation via velocity gradient partitioning

Di Zhou *, Rahul Arun †, Tim Colonius ‡, and H. Jane Bae §
California Institute of Technology, Pasadena, CA 91125, USA.

Wall-modeled large-eddy simulation (WMLES) has attracted significant attention in engineering applications as a high-fidelity simulation technique not limited by near-wall resolution requirements. It significantly reduces computational costs by resolving the energy-containing and dynamically important scales of turbulence far from the wall while modeling the effects of near-wall eddies. However, the inherent grid dependence of WMLES results raises the question of how to determine an adequate yet minimal resolution for the outer region. To address this question, we propose an approach to assess grid resolution that does not rely on *a priori* knowledge of domain-specific flow statistics. This approach leverages the velocity gradient partitioning, which provides an expressive, broadly applicable, and Galilean invariant description of local flow features. The error metric we define represents the deviation of the partitioning far from the wall in WMLES from the partitioning associated with isotropic turbulence. Using simulations of turbulent channel flow, we compare the convergence trends of this metric with those of conventional metrics representing turbulence kinetic energy errors. The partitioning metric effectively captures the response of resolved small-scale flow features to grid resolution and various other mesh and simulation parameters. It is particularly sensitive to the mesh-cell aspect ratio and subgrid-scale modeling; however, it is less sensitive to the friction Reynolds number and wall boundary conditions, which primarily impact large-scale flow features. Hence, the metric provides valuable and inexpensive insight into the sensitivity of small-scale flow features. While it alone cannot be used to holistically validate the accuracy of simulation results, coupling it with a metric that diagnoses large-scale flow features would provide a more complete picture. Beyond turbulent channel flow, preliminary results for flow over a Gaussian bump highlight the potential for the present approach to be applied to WMLES in more complex geometries.

I. Introduction

A. Grid resolution assessment in wall-modeled large-eddy simulation

High-fidelity numerical simulations of turbulent flows are becoming increasingly pragmatic due to advances in computing power and computational algorithms. Particularly, large-eddy simulation (LES) has enabled high-fidelity analyses of complex flows by resolving energetic and dynamically relevant turbulent scales while retaining modest computational costs compared to direct numerical simulation (DNS). However, for wall-bounded flows, the prohibitive computational costs incurred by resolving all relevant scales in near-wall turbulence have limited the ability of LES to inform many practical (e.g., industrial) applications. Wall-modeled LES (WMLES) provides a practical and efficient solution to this issue. It significantly reduces computational costs for wall-bounded flows by employing a reduced-order model on a relatively coarse computational mesh to represent the effects of energetic near-wall eddies. For example, recent studies [1, 2] have reported cost reductions of one to two orders of magnitude with respect to wall-resolved LES (WRLES) for attached flows over finite aspect ratio wings at various Reynolds numbers. WMLES has also been successfully applied to complex flow configurations in a broad range of practical engineering applications [3–5]. Therefore, coupled with computational advances, WMLES offers a promising avenue for enabling fast, low-cost, high-fidelity analyses of realistic engineering problems.

*Postdoctoral Scholar Research Associate in Aerospace, Graduate Aerospace Laboratories, AIAA Member
†Graduate Student, Graduate Aerospace Laboratories, AIAA Student Member
‡Frank and Ora Lee Marble Professor of Mechanical Engineering and Medical Engineering, Department of Mechanical and Civil Engineering, AIAA Associate Fellow
§Assistant Professor of Aerospace, Graduate Aerospace Laboratories, AIAA Senior Member

However, mesh generation remains a significant challenge in applying WMLES to the complex, three-dimensional geometries that characterize many applications of interest. Modern tools, such as the OpenFOAM® snappyHexMesh utility and the Cadence® Fidelity Voronoi-diagram-based mesh generator [6], can address this issue by generating self-similar and isotropic mesh elements around these geometries. Although these tools automate many aspects of mesh generation, determining appropriate grid resolution still relies heavily on domain expertise. Coupling mesh generators with solution-based mesh adaptation techniques offers a flexible approach to address this limitation. Regardless of how the mesh is generated, its design requires a robust approach to assess grid resolution. To be practically relevant, such an approach should employ metrics that (i) comprehensively reflect how well the mesh captures flow features of interest, (ii) do not depend on *a priori* knowledge of domain-specific flow statistics or higher-fidelity simulations, and (iii) can be applied to different flow configurations and solvers.

Various approaches for evaluating grid resolution and mesh quality in LES have been proposed. For example, the grid resolution can be compared with the Kolmogorov scale derived from separate Reynolds-averaged Navier–Stokes (RANS) simulations [7]; however, this approach depends strongly on the accuracy of RANS results. Another common approach evaluates grid resolution by characterizing LES errors in terms of a 'subgrid activity' parameter that captures the subgrid-scale (SGS) dissipation rate relative to the total dissipation rate [8]. Metrics based on the resolved and unresolved turbulence kinetic energy (TKE) have also been used to assess grid resolution in terms of both modeling and numerical errors [9–11]. Beyond purely statistical assessments, an approach based on the Lyapunov exponent has also been proposed [12] to characterize the ability of LES to capture dynamic processes inherent to turbulent flows. While these approaches provide valuable insights into LES errors and grid resolution, there is no general consensus on which approach is most appropriate for guiding mesh design for a particular application.

The fidelity of WMLES is sensitive to how well turbulent scales are resolved in the outer region (i.e., far from the wall). Therefore, there is a delicate balance between maintaining a resolution that is sufficiently fine to ensure accurate results but sufficiently coarse to be computationally feasible. In this setting, a metric that captures the effect of grid resolution on small-scale flow features would be particularly valuable. Velocity gradients provide a useful candidate for constructing such a metric since they reflect the local flow structure and capture ubiquitous features of small-scale turbulence [13, 14]. Based on this premise, the objective of the present study is to develop a metric that captures the effect of grid resolution on small-scale flow features using velocity gradients. Our approach exploits key advantages of the velocity gradient partitioning [15–17] based on a recently-developed normality-based decomposition of the velocity gradient tensor (VGT) [18–21].

B. Velocity gradient partitioning

The symmetry-based decomposition of the VGT, $\boldsymbol{A} = \boldsymbol{\nabla u}$, into the (symmetric) strain-rate tensor, $\boldsymbol{S} = \frac{1}{2}(\boldsymbol{A} + \boldsymbol{A}^{\mathrm{T}})$, and the (antisymmetric) vorticity tensor, $\boldsymbol{W} = \frac{1}{2}(\boldsymbol{A} - \boldsymbol{A}^{\mathrm{T}})$, is commonly employed in turbulence modeling. For example, in LES, eddy-viscosity models typically represent the effects of unclosed terms using the resolved strain-rate tensor. Moreover, many such models (e.g., the Smagorinsky model) express the eddy viscosity in terms of the strain-rate tensor [22–25]. However, despite its convenience and ubiquity in turbulence modeling, the symmetry-based decomposition provides relatively limited information about local flow features.

A recently-developed normality-based decomposition has emerged as a more expressive extension of the symmetry-based decomposition. This decomposition can be computed using the ordered real Schur form of the VGT [21] and it can be expressed as

$$\boldsymbol{A} = \boldsymbol{A}_\epsilon + \boldsymbol{A}_\varphi + \boldsymbol{A}_\gamma. \tag{1}$$

Here, $\boldsymbol{A}_\epsilon$, $\boldsymbol{A}_\varphi$, and $\boldsymbol{A}_\gamma$ represent normal straining (symmetric/normal), rigid rotation (antisymmetric/normal), and pure shearing (non-normal). This decomposition is related to the symmetry-based decomposition via $\boldsymbol{S} = \boldsymbol{A}_\epsilon + \boldsymbol{S}_\gamma$ and $\boldsymbol{W} = \boldsymbol{A}_\varphi + \boldsymbol{W}_\gamma$, where $\boldsymbol{S}_\gamma = \frac{1}{2}(\boldsymbol{A}_\gamma + \boldsymbol{A}_\gamma^{\mathrm{T}})$ and $\boldsymbol{W}_\gamma = \frac{1}{2}(\boldsymbol{A}_\gamma - \boldsymbol{A}_\gamma^{\mathrm{T}})$ are the symmetric and antisymmetric parts of pure shearing.

Using this decomposition, the strength of the velocity gradients can be partitioned as

$$A^2 = \mathrm{tr}\left(\boldsymbol{A}^{\mathrm{T}}\boldsymbol{A}\right) = A_\epsilon^2 + A_\varphi^2 + A_\gamma^2 + A_{\varphi\gamma}^2, \tag{2}$$

where A_ϵ^2, A_φ^2, and A_γ^2 represent the strengths of the constituents in Eq. (1) and $A_{\varphi\gamma}^2$ represents the interaction between shearing and rigid rotation. These strengths are all Galilean invariant quantities [16, 26]. Although the decomposition in Eq. (1) requires computation of a Schur decomposition, the partitioning in Eq. (2) can be computed directly from the eigendecomposition of the VGT [18–20]. Furthermore, Arun and Colonius [16] showed that the relative strengths of

normal straining, pure shearing, and the sum of rigid rotation and shear-rotation interactions can be determined as exact algebraic functions of the invariants of the VGT. Therefore, these contributions can be straightforwardly determined directly from the components of the VGT, which may be advantageous in modeling applications (like LES) that require rapid computations.

A primary advantage of the normality-based velocity gradient partitioning is its enhanced expressivity compared to the symmetry-based partitioning. This expressivity is particularly pronounced in the relative contributions of the constituents in Eq. (2) to the averaged velocity gradient strength. This averaged partitioning can be expressed as

$$\left\langle A_\zeta^2 \right\rangle_{A^2} = \left\langle A_\zeta^2 \right\rangle / \left\langle A^2 \right\rangle, \quad \zeta \in \{\epsilon, \varphi, \gamma, \varphi\gamma\}, \tag{3}$$

where $\langle \cdot \rangle$ represents averaging over homogeneous spatial directions and time (for stationary flows). In unbounded and wall-bounded flows with appropriate symmetries and boundary conditions, the strain rate and vorticity tensors are roughly (and sometimes exactly) equipartitioned in strength (i.e., $\left\langle S^2 \right\rangle_{A^2} \approx \left\langle W^2 \right\rangle_{A^2} \approx \frac{1}{2}$). By contrast, the normality-based partitioning can produce pronounced variations that capture the evolution across temporal regimes in transitional flows [16] and spatial regimes in sustained turbulence [17]. Moreover, the partitioning associated with isotropic turbulence has been shown to apply far from the wall in wall-bounded turbulence [17] and, to a lesser extent, for decaying turbulence [16]. The averaged partitioning statistics have also been shown to be relatively invariant with respect to the Reynolds number in isotropic turbulence [15] and in the nearly-isotropic regime of wall-bounded turbulence [17]. Arun and Colonius [16, 17] provide more comprehensive reviews of the advantages and applications of this partitioning and the VGT decomposition that produces it.

C. Outline of present study

The velocity gradient partitioning has the potential to address the need for a metric that captures the effect of grid resolution on small-scale flow features in WMLES. Its expressivity, broad applicability, and Galilean invariance are key advantages for assessing the statistical imprint of these flow features. Moreover, the reference partitioning associated with isotropic turbulence is well-known and does not require higher-fidelity simulations in complex flow configurations. Motivated by these advantages, the present study proposes a novel method for grid resolution assessment in WMLES based on the velocity gradient partitioning. We primarily evaluate its performance using WMLES of turbulent channel flow at moderately high friction Reynolds numbers, Re_τ, with an extension to WMLES of flow over a Gaussian bump in Appendix I. In the remainder of this paper, we discuss details of the simulations in Sec. II, introduce and evaluate the proposed grid resolution assessment method in Sec. III, and summarize the takeaways and outlook in Sec. IV.

II. Mesh and simulation parameters

The simulations in the present study are conducted using an LES code designed for incompressible flows [27]. The code employs a second-order accurate finite volume scheme that is low-dissipative, conserves kinetic energy, and solves the pressure Poisson equation using an algebraic multigrid method [28]. The LES code has been validated in a broad range of turbulent flows, including rough-wall turbulent boundary layers (TBLs) [29], flow over an axisymmetric body of revolution [30], and rotor interactions with a thick axisymmetric TBL [31].

We evaluate the proposed approach to grid resolution assessment using WMLES of turbulent channel flow between two flat plates. The computational domain measures $4\pi h \times 2h \times 2\pi h$ in the streamwise (x), wall-normal (y), and spanwise (z) directions, respectively, where h denotes the channel half-height, and periodic boundary conditions are applied in the x and z directions. All simulations maintain a maximum Courant–Friedrichs–Lewy number of 1.0. Each simulation is equilibrated by first prescribing a bulk velocity, $U_b = 1$, and subsequently switching to a constant imposed pressure gradient in the x direction, which remains until the end of the simulation. The initial 200 flow-through times are discarded to surpass the transient phase and the subsequent 100 flow-through times are used to obtain the velocity fields and the corresponding velocity gradients, which are evaluated at cell centers.

As outlined in Table 1, we conduct simulations employing various different mesh configurations. These meshes contain isotropic cells and anisotropic cells with different aspect ratios. For each mesh, the domain is uniformly discretized in the x, y, and z directions. We evaluate each mesh at four levels of resolution and the meshes have identical cell volumes at each level. We therefore define a characteristic mesh resolution using a geometric mean, $\Delta_g = \sqrt[3]{\Delta x \Delta y \Delta z}$, where Δx, Δy, and Δz denote the mesh-cell sizes in the x, y, and z directions, respectively.

Table 1 Computational mesh parameters for the present channel flow simulations, including the number of cells (N_x, N_y, N_z) and the cell sizes (Δx, Δy, Δz) in each direction.

Case	(N_x, N_y, N_z)	$\Delta x/h$	$\Delta y/h$	$\Delta z/h$
IM1	(74, 12, 37)	1.7×10^{-1}	1.7×10^{-1}	1.7×10^{-1}
IM2	(148, 24, 74)	8.5×10^{-2}	8.5×10^{-2}	8.5×10^{-2}
IM3	(296, 48, 148)	4.2×10^{-2}	4.2×10^{-2}	4.2×10^{-2}
IM4	(592, 96, 296)	2.1×10^{-2}	2.1×10^{-2}	2.1×10^{-2}
AM-a1	(74, 32, 14)	1.7×10^{-1}	6.2×10^{-2}	4.5×10^{-1}
AM-a2	(148, 64, 28)	8.5×10^{-2}	3.1×10^{-2}	2.2×10^{-1}
AM-a3	(296, 128, 56)	4.2×10^{-2}	1.6×10^{-2}	1.1×10^{-1}
AM-a4	(592, 256, 112)	2.1×10^{-2}	7.8×10^{-3}	5.6×10^{-2}
AM-b1	(28, 32, 37)	4.5×10^{-1}	6.2×10^{-2}	1.7×10^{-1}
AM-b2	(56, 64, 74)	2.2×10^{-1}	3.1×10^{-2}	8.5×10^{-2}
AM-b3	(112, 128, 148)	1.1×10^{-1}	1.6×10^{-2}	4.2×10^{-2}
AM-b4	(224, 256, 296)	5.6×10^{-2}	7.8×10^{-3}	2.1×10^{-2}

In addition to the mesh configuration, we also consider the effect of the friction Reynolds number, wall boundary conditions, and SGS modeling on the LES error metrics. We consider two different friction Reynolds numbers, $\mathrm{Re}_\tau \approx 1000$ and $\mathrm{Re}_\tau \approx 2000$, in the present study. We also consider two different wall boundary conditions: (i) the no-slip boundary condition and (ii) the equilibrium stress wall model (EQWM) [32], which provides an approximate wall-shear stress boundary condition. For the EQWM cases, the matching location of the wall model is set at the center of the fourth off-wall cell. The value of Re_τ is more sensitive to the grid resolution for the no-slip boundary condition than for the EQWM (see Appendix II for more details). The effect of the unresolved motions is modeled using three SGS models based on the eddy-viscosity assumption. These models include the dynamic Smagorinsky model (DSM) [22, 23], the Vreman model [24], and the anisotropic minimum dissipation (AMD) model [25]. For the Vreman model, the model constant is set to 0.025, as recommended for complex wall-bounded turbulence [24]. For the AMD model, the model constant is set to 0.3 and determined solely by the choice of numerical method [25].

III. Results and Discussion

A. Grid resolution assessment via velocity gradient partitioning

The metric we introduce for assessing grid resolution in WMLES is based on the velocity gradient partitioning discussed in Sec. I.B. The partitioning is relatively easy to implement and provides an expressive, broadly applicable, and Galilean invariant means of evaluating the effects of mesh and simulation parameters. Moreover, since velocity gradients capture local flow features, we expect our approach to be particularly sensitive to mesh-cell parameters since they operate at the smallest resolved scales. This sensitivity complements conventional approaches, which are typically sensitive to parameters that influence larger-scale flow features.

Arun and Colonius [16] showed that the partitioning in channels and boundary layers at sufficiently high friction Reynolds numbers collapses onto the isotropic partitioning far from the wall, where the mean shearing is relatively weak. Based on this finding, we define the deviation of the partitioning in the outer region from the isotropic partitioning as a metric to assess grid resolution in WMLES. For the present channel flow simulations, this metric can be expressed as

$$\varepsilon_{A^2} = \frac{\displaystyle\int_{0.3h}^{h} \sum_{\zeta \in \{\epsilon,\varphi,\gamma,\varphi\gamma\}} \left| \left\langle A_\zeta^2 \right\rangle_{A^2} - \left\langle A_\zeta^2 \right\rangle_{A^2}^{iso} \right| dy}{\displaystyle\int_{0.3h}^{h} \sum_{\zeta \in \{\epsilon,\varphi,\gamma,\varphi\gamma\}} \left| \left\langle A_\zeta^2 \right\rangle_{A^2}^{iso} \right| dy}, \tag{4}$$

where $\left\langle A_\zeta^2 \right\rangle_{A^2}^{iso}$ denotes the isotropic partitioning and $|\cdot|$ denotes the absolute value. Since the integrand in the denominator evaluates to unity, the metric averages the absolute deviations expressed in the numerator from the top

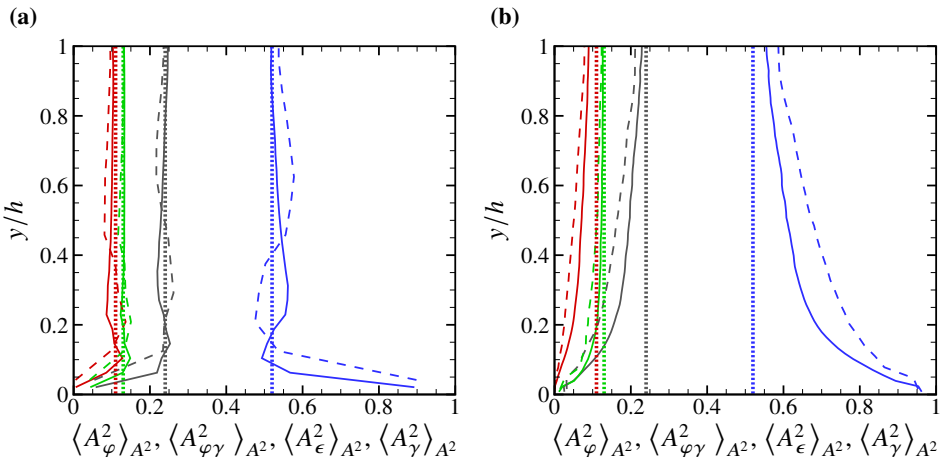

Fig. 1 Velocity gradient partitioning profiles for WMLES of turbulent channel flow at $\mathrm{Re}_\tau \approx 1000$ on isotropic-cell (a) and anisotropic-cell meshes (b). In (a), the dashed and solid lines represent cases IM2 and IM3, respectively, and, in (b), they represent cases AM-a2 and AM-a3, respectively (see Table 1). All cases shown employ the DSM in the interior and the EQWM at the wall. The vertical dotted lines indicate the isotropic partitioning values [17] and the black, red, blue, and green curves denote $\langle A_\epsilon^2 \rangle_{A^2}$, $\langle A_\varphi^2 \rangle_{A^2}$, $\langle A_\gamma^2 \rangle_{A^2}$, and $\langle A_{\varphi\gamma}^2 \rangle_{A^2}$, respectively.

of the log-law region ($y/h = 0.3$) to the channel centerline ($y/h = 1$). The integration limits capture a region where the partitioning (from DNS) collapses onto the isotropic partitioning [17] and they are intentionally expressed in outer units. We use the reference isotropic partitioning values reported by Arun and Colonius [17], which are consistent with those reported by Das and Girimaji [15]. These reference values are given by $\langle A_\epsilon^2 \rangle_{A^2}^{iso} = 0.240$, $\langle A_\varphi^2 \rangle_{A^2}^{iso} = 0.106$, $\langle A_\gamma^2 \rangle_{A^2}^{iso} = 0.520$, and $\langle A_{\varphi\gamma}^2 \rangle_{A^2}^{iso} = 0.134$.

It is important to ensure that the reference partitioning statistics are consistent with expectations for the resolved small-scale flow features in WMLES. For example, eddy-viscosity models have been shown to produce velocity gradient statistics and structures that mimic those of an unfiltered DNS [33, 34]. Since we only consider eddy viscosity models in the present study, we therefore use the velocity gradient partitioning values from an unfiltered DNS of forced isotropic turbulence as our reference for evaluating the mesh resolution for WMLES. However, other SGS models, like mixed models, are known to instead reproduce the velocity gradient statistics of an analogously filtered DNS [33, 34]. In these cases, it would likely be more appropriate to use the filtered partitioning as the baseline. Therefore, while the choice of SGS model is typically based on the reproducing flow features and statistics of interest (e.g., dissipation, energy transfer, etc.), the choice of evaluation metric should be tailored to the selected SGS model if it is based on velocity gradient statistics.

Fig. 1 shows the velocity gradient partitioning profiles for WMLES of channel flow at $\mathrm{Re}_\tau \approx 1000$ using isotropic-cell and anisotropic-cell meshes with various resolutions. Consistent with the findings of Arun and Colonius [17], the partitioning approaches the isotropic partitioning far from the wall even for WMLES. Moreover, the partitioning in the outer region is much closer to the isotropic partitioning (i) when the mesh resolution is finer and (ii) when the mesh cells are isotropic (as opposed to anisotropic). These results qualitatively validate our expectation that the unfiltered isotropic partitioning is an appropriate baseline for the present study. They also illustrate that the partitioning is sensitive to variations in mesh parameters that influence resolved small-scale flow features.

As discussed in Sec. I, mesh assessment and design is often critical for simulating flows in more complex geometries. In Appendix I, we demonstrate the applicability of our approach to a more complex flow configuration by evaluating the partitioning in a WMLES of flow over a two-dimensional Gaussian bump. The results demonstrate that the partitioning collapses onto the isotropic values in the outer region even at locations that exhibit strong adverse/favorable pressure gradients and separation/reattachment. They further support the use of the (unfiltered) isotropic partitioning as a baseline for the eddy-viscosity models considered in the present study and they serve as a proof-of-concept for extensions to non-canonical flow configurations.

B. Grid resolution assessment for turbulent channel flow

We evaluate the sensitivity of the metric proposed in Eq. (4) to various parameters of the channel flow simulations, including the friction Reynolds number, wall boundary conditions, SGS model, and mesh configuration. For comparison, we use the streamwise, spanwise, and wall-normal TKE errors in the outer region to characterize the sensitivity of flow statistics associated with larger-scale flow features. The streamwise TKE error is defined as

$$\varepsilon_{u^2} = \left[\frac{\displaystyle\int_{0.3h}^{h} \left(\frac{\langle u'u' \rangle}{U_b^2} - \frac{\langle u'u' \rangle_{DNS}}{U_{b,DNS}^2} \right)^2 dy}{\displaystyle\int_{0.3h}^{h} \left(\frac{\langle u'u' \rangle_{DNS}}{U_{b,DNS}^2} \right)^2 dy} \right]^{1/2}, \tag{5}$$

where u' denotes the fluctuating streamwise velocity and the subscript $(\cdot)_{DNS}$ denotes data obtained from a DNS of turbulent channel flow at the same Reynolds number [35]. Analogous metrics, ε_{v^2} and ε_{w^2}, are defined for the wall-normal and spanwise TKE errors, respectively. The integration range matches the range in Eq. (4) and it is slightly smaller than that considered in Eq. (25) of [36]. We normalize the velocity fluctuations by the bulk velocities since the bulk Reynolds numbers are nearly identical for the present LES and DNS cases. Further, since $U_b \approx U_{b,DNS} \approx 1$, the integrands in Eq. (4) approximate those considered in Eq. (25) of [36]. Another option would be to normalize by the friction velocities, but this makes the error metric sensitive to impact of the different wall boundary conditions (see Appendix II). With either normalization, the error would approach zero when the LES resolution approaches that of DNS since both the bulk and friction Reynolds numbers for LES would match those for DNS.

Fig. 2 shows how ε_{A^2}, ε_{u^2}, ε_{v^2}, and ε_{w^2} vary with Δ_g/h for WMLES of channel flow at two different friction Reynolds numbers, $\mathrm{Re}_\tau \approx 1000$ and $\mathrm{Re}_\tau \approx 2000$. The TKE errors are sensitive to Re_τ, and they increase with increasing Re_τ. By contrast, the velocity gradient partitioning error is insensitive to Re_τ. These results reflect that the partitioning is primarily sensitive to the resolved small-scale flow features, whereas the TKE reflects contributions from larger scales in the outer region (which are more sensitive to Re_τ). These results are consistent with previous findings, which suggest that TKE errors are typically associated with large-scale flow structures in WMLES [37].

Fig. 3 compares the error scalings for each metric using the no-slip boundary condition and the EQWM. The TKE errors are also sensitive to the wall boundary conditions, with the EQWM reducing errors significantly compared to the no-slip boundary condition. This sensitivity is even more pronounced for the TKE error metric that normalizes velocity fluctuations by the friction velocity (see Appendix II). By contrast, the partitioning error is only mildly impacted by the wall boundary condition at each level of resolution. These results are consistent with those in Fig. 2, and they reflect that small-scale flow structures in the outer region are less sensitive to the wall model than large-scale flow structures in the outer region [37]. Together, Figs. 2 and 3 highlight that the velocity gradient partitioning metric is relatively insensitive to parameters that primarily affect large-scale flow features in the outer region, like the friction Reynolds number and wall boundary conditions. As such, while the partitioning metric should not be used to evaluate the impact of these parameters, it has the potential to distinguish sensitivities to parameters that more strongly impact small-scale flow features.

Fig. 4 compares the error scalings for each metric using the different eddy-viscosity SGS models, including the DSM, the Vreman model, and the AMD model. For relatively coarse meshes, the different SGS models produce different velocity gradient partitioning errors. However, the partitioning errors for these models collapse as resolution increases since the effect of the SGS motions is diminished. Moreover, the partitioning error scalings capture important qualitative features observed in the TKE error scalings, such as the non-monotonic convergence for the Vreman model. Therefore, for a given model, the partitioning error scaling may be a useful proxy for the TKE error scaling. However, the partitioning error does not directly reflect how the TKE errors compare quantitatively to one another for different models. Therefore, while it should not be used to compare the impact of different SGS models on large-scale flow features, it provides a valuable comparison of how well each model captures small-scale flow features.

Fig. 5 compares the error scalings for each metric using different mesh-cell aspect ratios, including both isotropic and anisotropic cells. The values of Δ_g/h are identical for each case since the isotropic and anisotropic cells all share the same volume. Consistent with the results in Fig. 1(b), the partitioning error is sensitive to the mesh-cell aspect ratio. The partitioning error increases significantly for anisotropic-cell meshes, especially for the AM-b meshes, which are elongated in the streamwise direction and compressed in the wall-normal direction (see Table 1). These results are insensitive to the grid resolution definition for anisotropic meshes (see Appendix III). By contrast, the TKE errors are typically largest for the AM-a meshes, which are elongated in the spanwise direction and compressed in the wall-normal direction. Therefore, while streamwise-elongated meshes may be useful for capturing typical large-scale flow features,

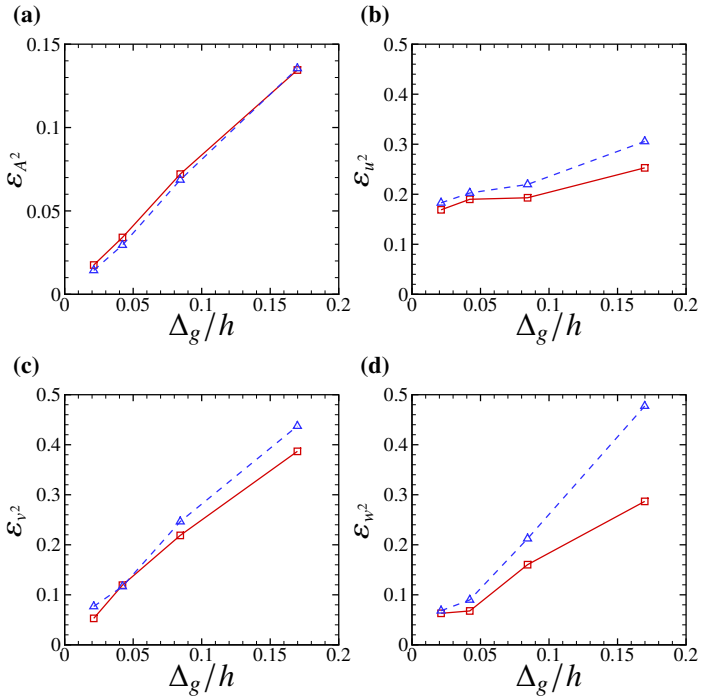

Fig. 2 Error scalings for the velocity gradient partitioning (a) and the streamwise (b), wall-normal (c), and spanwise (d) TKE. All simulations employ isotropic-cell meshes, the DSM, and the EQWM. Solid red and dashed blue lines represent $\mathrm{Re}_\tau \approx 1000$ and $\mathrm{Re}_\tau \approx 2000$, respectively.

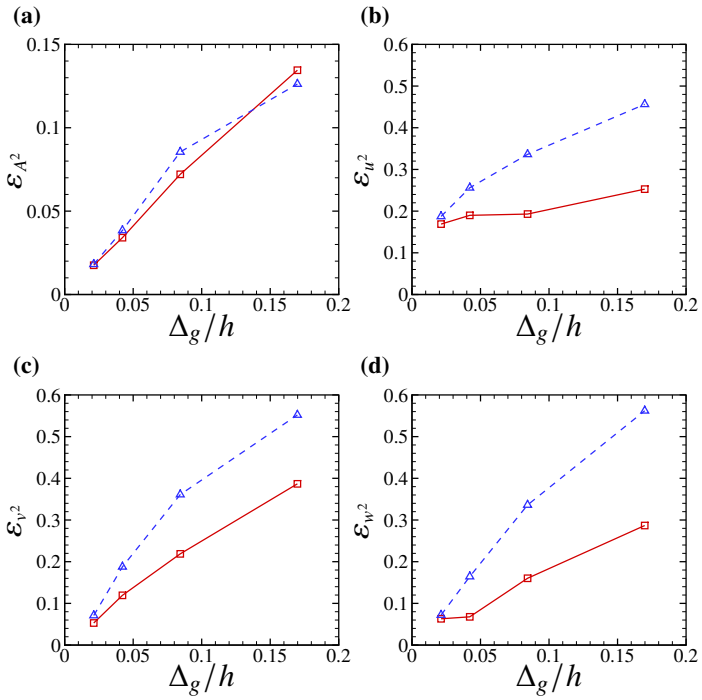

Fig. 3 Error scalings as in Fig. 2. All simulations are run at $\mathrm{Re}_\tau \approx 1000$ and they employ isotropic-cell meshes and the DSM. Solid red and dashed blue lines represent the EQWM and no-slip boundary conditions, respectively.

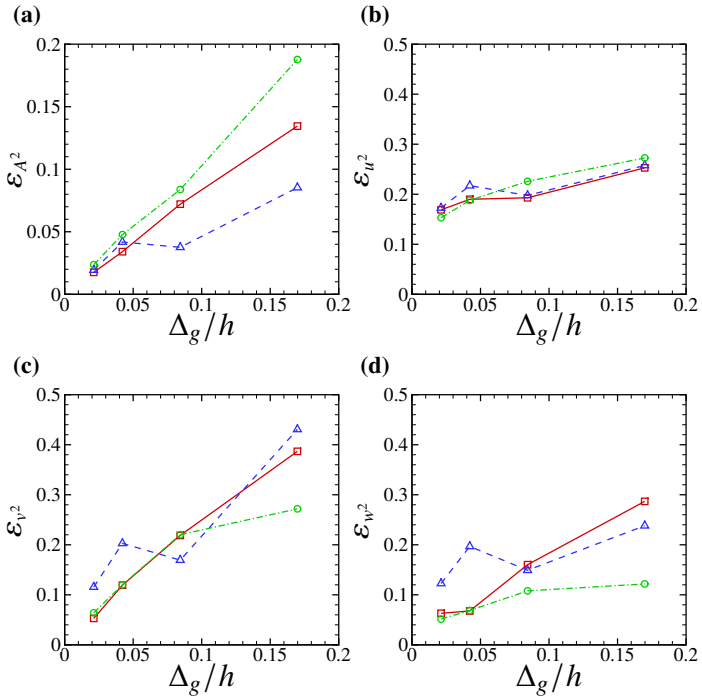

Fig. 4 Error scalings as in Fig. 2. All simulations are run at $\mathrm{Re}_\tau \approx 1000$ and they employ isotropic-cell meshes and the EQWM. Solid red, dashed blue, and dash-dotted green lines represent the DSM, the Vreman model, and the AMD model, respectively.

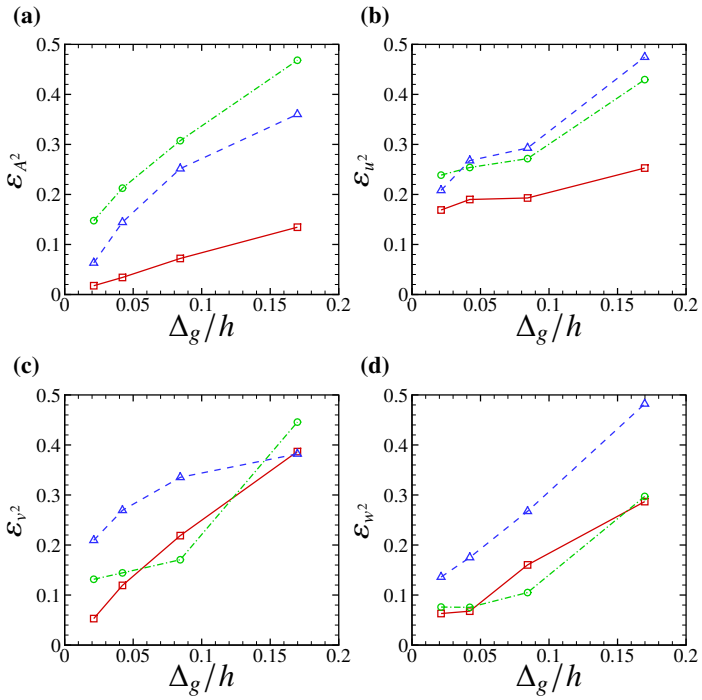

Fig. 5 Error scalings as in Fig. 2. All simulations are run at $\mathrm{Re}_\tau \approx 1000$ and they employ the DSM and the EQWM. Solid red, dashed blue, and dash-dotted green lines represent the IM, AM-a, and AM-b cases, respectively.

they may not capture as well small-scale flow features associated with the resolved velocity gradients. Similar to Fig. 4, these results highlight the role of the partitioning metric in evaluating the resolved small-scale flow features. They therefore complement the results of previous studies [36–38], which considered the sensitivity of velocity statistics that primarily reflect large-scale flow features. Moving forward, disentangling how the different mesh configurations affect (i) the computation of the velocity gradients and (ii) SGS modeling may provide further insight into the error scalings observed in Fig. 5.

IV. Conclusions

We propose a novel method to assess grid resolution in WMLES. This method is based on the normality-based velocity gradient partitioning, which identifies the relative contributions of normal straining, rigid rotation, pure shearing, and shear-rotation correlations to the strength of velocity gradients. For wall-bounded flows, these relative contributions collapse onto those associated with isotropic turbulence in the outer region of the flow, where the mean shearing is relatively weak. Leveraging this feature, we use the deviation from the isotropic partitioning in the outer region as an error metric to assess grid resolution in WMLES. This metric is tailored to characterize how well a given simulation can capture expected small-scale flow features far from the wall.

Using channel flow simulations, we evaluate the sensitivity of this metric to various mesh and simulation parameters. Since the partitioning error metric captures variations in small-scale flow features, it is highly sensitive to SGS modeling and the mesh-cell aspect ratio, which are directly tied to grid resolution. By contrast, it is less sensitive to the friction Reynolds number and wall boundary conditions, which primarily impact larger-scale flow features. Beyond capturing qualitative convergence trends, the metric provides key insights into the effect of SGS modeling and mesh-cell aspect ratio that go beyond conventional analyses of TKE. These results have the potential to inform the design of WMLES meshes that appropriately capture resolved small-scale flow features and their statistics. While we do not propose a strict threshold for resolving these features, a partitioning error of less than 5% seems reasonable for initial assessments of grid resolution.

The expressivity, broad applicability, and Galilean invariance of the proposed metric suggest it may be useful for designing, assessing, and adapting meshes in more complex flow configurations. One particular advantage of this metric for such flows is that it does not require *a priori* knowledge of domain-specific flow statistics obtained from high resolution simulations. We provide preliminary evidence of this advantage by showing that the isotropic partitioning also applies to the velocity gradients far from the wall in a WMLES of flow over a Gaussian bump, which includes regions of separation and reattachment. Although the proposed metric is only applied to WMLES in the current study, it also has the potential to assess grid resolution in WRLES. However, while this metric provides insight into the resolution of small-scale flow features, it cannot be used to holistically capture the impact of mesh and simulation parameters on large-scale flow features and statistics. Moreover, while the reference partitioning statistics we use are appropriate for eddy-viscosity models, they must be tailored to reflect the behavior of the SGS model of interest. As such, investigations of the proposed metric in more complex flow configurations, with other SGS models, and in conjunction with complementary metrics would entail useful future work.

Appendix I: Velocity gradient partitioning for flow over a Gaussian bump

To demonstrate the applicability of our approach to more complex wall-bounded turbulent flows, we compute the velocity gradient partitioning using a well-resolved WMLES of flow over a two-dimensional Gaussian bump [38]. This configuration mimics smooth junctions, such as those between the wing and fuselage of an aircraft. The flow involves smooth-body separation of a TBL subject to pressure-gradient and surface-curvature effects. Fig. 6 depicts the instantaneous streamwise velocity, u_x, in an $x-y$ plane obtained from a snapshot of the WMLES. A thin zero-pressure-gradient (ZPG) flat-plate TBL enters the inlet at $x/L = -0.85$, where L denotes the bump width. The boundary layer gradually accelerates along the windward side of the bump, reaching a maximum velocity near the peak. Downstream, the flow decelerates over the leeward side, causing rapid boundary layer thickening and a significant separation bubble, which reattaches near the edge of the bump's leeward side. The Reynolds number based on the freestream velocity (U_∞) and bump width is $\mathrm{Re}_L = 2 \times 10^6$. The friction Reynolds number, based on the local boundary-layer thickness and friction velocity, ranges from $\mathrm{Re}_\tau \approx 800$ to $\mathrm{Re}_\tau \gtrsim 8000$.

The WMLES was conducted on a hybrid mesh with 993 million cells using the same flow solver as the present study (see Sec. II). It employed the Vreman model [24] with a model constant of 0.025 to represent the effect of the SGS motions. For the bottom boundary, it applied an ideal wall model that incorporates the mean wall-shear stress

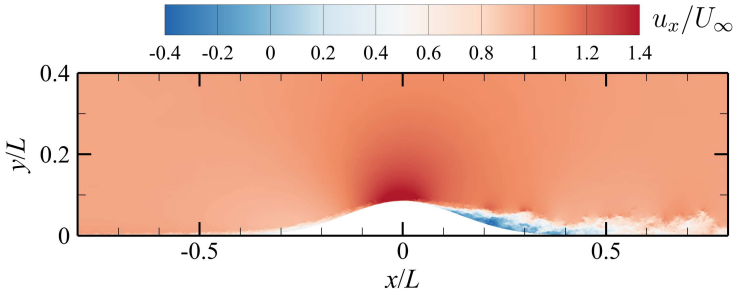

Fig. 6 Instantaneous streamwise velocity, u_x/U_∞, in the $x-y$ plane at $z/L=0$ for the WMLES of flow over a two-dimensional Gaussian bump at $\mathrm{Re}_L = 2\times10^6$.

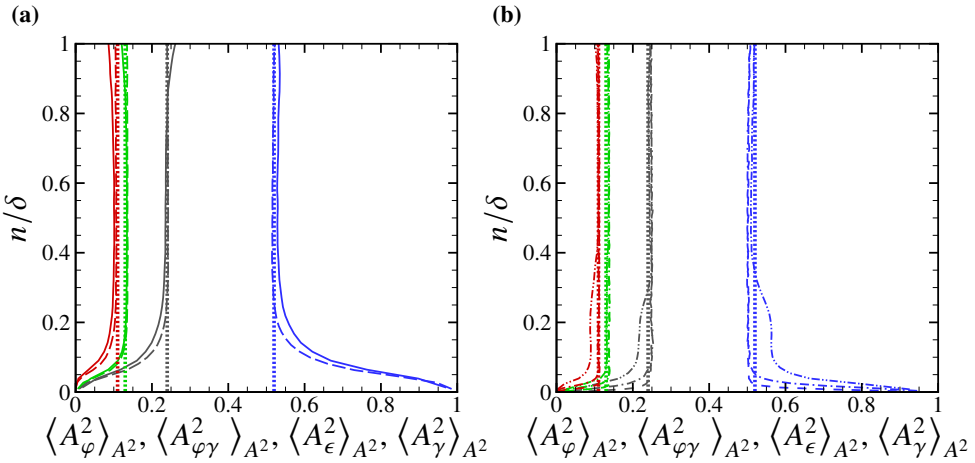

Fig. 7 Velocity gradient partitioning profiles for the WMLES of flow over a two-dimensional Gaussian bump at $\mathrm{Re}_L = 2\times10^6$. In (a), the solid and long-dashed lines represent the results at $x/L=-0.7$ and $x/L=-0.2$, respectively. In (b) the dash-dot-dotted, dash-dotted, and dashed lines represent the results at $x/L=0.05$, $x/L=0.2$, $x/L=0.4$. The vertical dotted lines indicate the isotropic partitioning values [17] and the black, red, blue, and green curves denote $\langle A_\epsilon^2\rangle_{A^2}$, $\langle A_\varphi^2\rangle_{A^2}$, $\langle A_\gamma^2\rangle_{A^2}$, and $\langle A_{\varphi\gamma}^2\rangle_{A^2}$, respectively.

obtained from a DNS of the same configuration. The WMLES accurately predicts of key flow features, including the separation bubble on the bump's leeward side. Zhou and Bae [38] provide a detailed description of the simulation setup and an assessment of its fidelity.

In Fig. 7(a), we show partitioning profiles as a function of the wall-normal coordinate (n) for two stations located upstream of the bump peak. The first station ($x/L=-0.7$) lies in the flat-plate region under ZPG and the second station ($x/L=-0.2$) is on the windward side of the bump, where the favorable pressure gradient is strong. The partitioning at these locations collapses well onto the isotropic partitioning above 30% of the local TBL thickness, δ (i.e., for $n/\delta \gtrsim 0.3$). However, the partitioning at $x/L=-0.7$ begins to diverge from these values near the edge of the boundary layer, which represents the transition to a potential flow near the freestream [17]. Fig. 7(b) shows results at three locations downstream of the bump peak. The first ($x/L=0.05$) is located in the region with a strong adverse pressure gradient, the second ($x/L=0.2$) is located within the separation bubble, and the third ($x/L=0.4$) is located downstream of the reattachment point. At each of these downstream locations, the partitioning again collapses well onto the isotropic partitioning for $n/\delta \gtrsim 0.3$. At locations within the separation bubble and downstream of reattachment, this collapse extends even closer to the wall. Altogether, these results indicate that the isotropic partitioning is broadly applicable in the outer region of TBLs even when complex geometry induces pressure gradients that can lead to separation and reattachment.

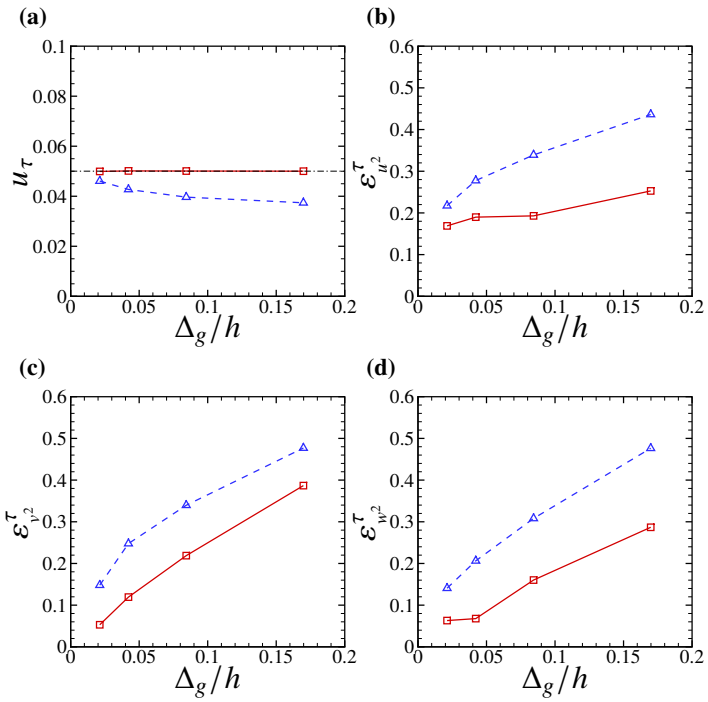

Fig. 8 Friction velocities (a) and error scalings for the streamwise (b), wall-normal (c), and spanwise (d) TKE based on the metric in Eq.(6). All simulations are run at $\mathrm{Re}_\tau \approx 1000$ and they employ isotropic-cell meshes and the DSM. Solid red and dashed blue lines represent the EQWM and no-slip boundary conditions, respectively. In (a), the dash-dotted black line denotes the friction velocity from DNS [35].

Appendix II: Turbulence kinetic energy error scalings normalized by friction velocity

The TKE error metric defined in Eq. (5) normalizes the velocity fluctuations using bulk velocities. Here, we instead normalize the velocity fluctuations using friction velocities. The corresponding streamwise TKE error is defined as

$$\varepsilon^\tau_{u^2} = \left[\frac{\displaystyle\int_{0.3h}^{h} \left(\frac{\langle u'u' \rangle}{u_\tau^2} - \frac{\langle u'u' \rangle_{DNS}}{u^2_{\tau,DNS}} \right)^2 dy}{\displaystyle\int_{0.3h}^{h} \left(\frac{\langle u'u' \rangle_{DNS}}{u^2_{\tau,DNS}} \right)^2 dy} \right]^{1/2}, \tag{6}$$

where u_τ denotes the friction velocity. Analogous metrics, $\varepsilon^\tau_{v^2}$ and $\varepsilon^\tau_{w^2}$, are defined for the wall-normal and spanwise TKE errors, respectively. Since the friction velocity is sensitive to the effects of the wall boundary conditions, these effects contribute to the TKE error metric defined in Eq. (6).

Fig. 8(a) shows the friction velocities obtained from simulations with isotropic-cell meshes and the DSM under different wall boundary conditions. While the EQWM accurately captures the wall-shear stress from DNS, the wall-shear stress is reduced when employing the no-slip boundary condition (especially for the coarser meshes). The TKE error scalings in Figs. 8(b-d) are analogous to those in Fig. 3 but employ the metric in Eq. (6). Since the EQWM accurately reproduces the wall-shear stress, it is not significantly impacted by the u_τ normalization. Although not shown here, this is also true for simulations involving different mesh configurations, friction Reynolds numbers, and SGS models. By contrast, the TKE errors for the no-slip boundary condition are larger than those in Fig. 3 since the no-slip boundary condition less accurately captures the wall-shear stress. These larger errors highlight that normalizing by u_τ makes the TKE error metrics more sensitive to the wall boundary conditions.

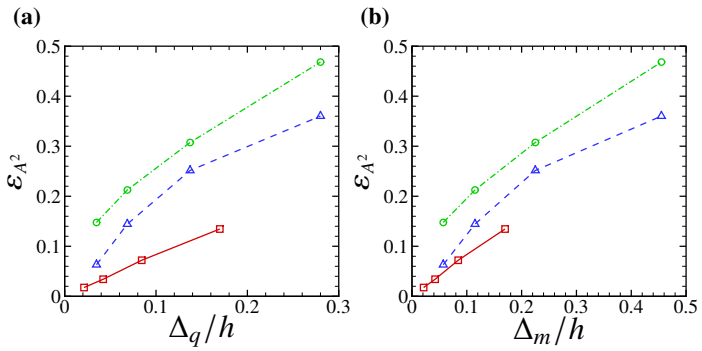

Fig. 9 Error scalings from Fig. 5 plotted in terms of the quadratic-mean mesh-cell size (Δ_q) in (a) and the maximum mesh-cell size (Δ_m) in (b).

Appendix III: Partitioning error scalings with alternative grid resolution definitions

While Figs. 2–5 show error scalings in terms of Δ_g, which is based on the geometric mean cell size, alternative definitions of the cell size can be used for anisotropic meshes. Here, we complement the results in Fig. 5 by characterizing the error scalings for the isotropic and anisotropic meshes using two alternative definitions for the grid resolution. In Fig. 9(a), we plot the error scalings using the quadratic mean of the mesh-cell sizes, $\Delta_q = \sqrt{(\Delta x^2 + \Delta y^2 + \Delta z^2)/3}$. In Fig. 9(b), we plot them using the maximum of the mesh-cell sizes, $\Delta_m = \max(\Delta x, \Delta y, \Delta z)$. The results for these two definitions are qualitatively similar to those in Fig. 5, but the error curves are slightly closer to one another when using Δ_m. Overall, these results further support the conclusion that anisotropic meshes have noticeable impacts on small-scale flow features that are distinct from the impacts on large-scale flow features in WMLES.

Acknowledgments

D.Z. and H.J.B. acknowledge the support by the National Science Foundation (NSF) under grant No. 2152705 and by the Office of Naval Research under grant No. N00014-23-1-2729. R.A. was supported by the Department of Defense (DoD) through the National Defense Science and Engineering Graduate (NDSEG) Fellowship Program. Computational resources were provided by the Discover project at Pittsburgh Supercomputing Center through allocation PHY240020 from the Advanced Cyberinfrastructure Coordination Ecosystem: Services & Support (ACCESS) program, which is supported by NSF grants No. 2138259, No. 2138286, No. 2138307, No. 2137603, and No. 2138296. R.A. gratefully acknowledges P.L. Johnson and M. Kamal for insightful discussions.

References

[1] Choi, H., and Moin, P., "Grid-point requirements for large eddy simulation: Chapman's estimates revisited," *Physics of Fluids*, Vol. 24, No. 1, 2012. https://doi.org/10.1063/1.3676783.

[2] Yang, X. I. A., and Griffin, K. P., "Grid-point and time-step requirements for direct numerical simulation and large-eddy simulation," *Physics of Fluids*, Vol. 33, No. 1, 2021. https://doi.org/10.1063/5.0036515.

[3] Lehmkuhl, O., Park, G. I., Bose, S. T., and Moin, P., "Large-eddy simulation of practical aeronautical flows at stall conditions," *Proceedings of the 2018 Summer Program, Center for Turbulence Research, Stanford University*, 2018, pp. 87–96. https://web.stanford.edu/group/ctr/Summer/SP18/reports/II_Numerical_Methods/02_Lehmkuhl.pdf.

[4] Lozano-Durán, A., and Bae, H. J., "Machine learning building-block-flow wall model for large-eddy simulation," *Journal of Fluid Mechanics*, Vol. 963, 2023, p. A35. https://doi.org/10.1017/jfm.2023.331.

[5] Goc, K. A., Moin, P., Bose, S. T., and Clark, A. M., "Wind tunnel and grid resolution effects in large-eddy simulations of the high-lift common research model," *Journal of Aircraft*, Vol. 61, No. 1, 2024, pp. 267–279. https://doi.org/10.2514/1.C037238.

[6] Brès, G. A., Ivey, C. B., Philips, D. A., Bose, S., Teramura, M., Moriya, T., and Ambo, K., "Large-eddy simulations of multi-bladed VTOL rotors for air vehicle aeroacoustic predictions," *AIAA Aviation 2023 Forum*, p. 2023-3938. https://doi.org/10.2514/6.2023-3938.

[7] Gant, S. E., "Reliability issues of LES-related approaches in an industrial context," *Flow, Turbulence and Combustion*, Vol. 84, 2010, pp. 325–335. https://doi.org/10.1007/s10494-009-9237-8.

[8] Geurts, B. J., and Fröhlich, J., "A framework for predicting accuracy limitations in large-eddy simulation," *Physics of Fluids*, Vol. 14, No. 6, 2002, pp. L41–L44. https://doi.org/10.1063/1.1480830.

[9] Celik, I. B., Cehreli, Z. N., and Yavuz, I., "Index of resolution quality for large eddy simulations," *Journal of Fluids Engineering*, Vol. 127, No. 5, 2005, pp. 949–958. https://doi.org/10.1115/1.1990201.

[10] Klein, M., "An attempt to assess the quality of large eddy simulations in the context of implicit filtering," *Flow, Turbulence and Combustion*, Vol. 75, 2005, pp. 131–147. https://doi.org/10.1007/s10494-005-8581-6.

[11] Benard, P., Balarac, G., Moureau, V., Dobrzynski, C., Lartigue, G., and D'Angelo, Y., "Mesh adaptation for large-eddy simulations in complex geometries," *International Journal for Numerical Methods in Fluids*, Vol. 81, No. 12, 2016, pp. 719–740. https://doi.org/10.1002/fld.4204.

[12] Nastac, G., Labahn, J. W., Magri, L., and Ihme, M., "Lyapunov exponent as a metric for assessing the dynamic content and predictability of large-eddy simulations," *Physical Review Fluids*, Vol. 2, No. 9, 2017, p. 094606. https://doi.org/10.1103/PhysRevFluids.2.094606.

[13] Meneveau, C., "Lagrangian dynamics and models of the velocity gradient tensor in turbulent flows," *Annual Review of Fluid Mechanics*, Vol. 43, 2011, pp. 219–245. https://doi.org/10.1146/annurev-fluid-122109-160708.

[14] Johnson, P. L., and Wilczek, M., "Multiscale velocity gradients in turbulence," *Annual Review of Fluid Mechanics*, Vol. 56, 2024, pp. 463–490. https://doi.org/10.1146/annurev-fluid-121021-031431.

[15] Das, R., and Girimaji, S. S., "Revisiting turbulence small-scale behavior using velocity gradient triple decomposition," *New Journal of Physics*, Vol. 22, No. 6, 2020, p. 063015. https://doi.org/10.1088/1367-2630/ab8ab2.

[16] Arun, R., and Colonius, T., "Velocity gradient analysis of a head-on vortex ring collision," *Journal of Fluid Mechanics*, Vol. 982, 2024, p. A16. https://doi.org/10.1017/jfm.2024.90.

[17] Arun, R., and Colonius, T., "Velocity gradient partitioning in turbulent flows," *Journal of Fluid Mechanics*, Vol. 1000, 2024, p. R5. https://doi.org/10.1017/jfm.2024.1021.

[18] Liu, C., Gao, Y., Tian, S., and Dong, X., "Rortex—A new vortex vector definition and vorticity tensor and vector decompositions," *Physics of Fluids*, Vol. 30, No. 3, 2018, p. 035103. https://doi.org/10.1063/1.5023001.

[19] Gao, Y., and Liu, C., "Rortex and comparison with eigenvalue-based vortex identification criteria," *Physics of Fluids*, Vol. 30, No. 8, 2018, p. 085107. https://doi.org/10.1063/1.5040112.

[20] Gao, Y., and Liu, C., "Rortex based velocity gradient tensor decomposition," *Physics of Fluids*, Vol. 31, No. 1, 2019, p. 011704. https://doi.org/10.1063/1.5084739.

[21] Kronborg, J., and Hoffman, J., "The triple decomposition of the velocity gradient tensor as a standardized real Schur form," *Physics of Fluids*, Vol. 35, No. 3, 2023, p. 031703. https://doi.org/10.1063/5.0138180.

[22] Germano, M., Piomelli, U., Moin, P., and Cabot, W. H., "A dynamic subgrid-scale eddy viscosity model," *Physics of Fluids A: Fluid Dynamics*, Vol. 3, No. 7, 1991, pp. 1760–1765. https://doi.org/10.1063/1.857955.

[23] Lilly, D. K., "A proposed modification of the Germano subgrid-scale closure method," *Physics of Fluids A: Fluid Dynamics*, Vol. 4, No. 3, 1992, pp. 633–635. https://doi.org/10.1063/1.858280.

[24] Vreman, A. W., "An eddy-viscosity subgrid-scale model for turbulent shear flow: Algebraic theory and applications," *Physics of Fluids*, Vol. 16, No. 10, 2004, pp. 3670–3681. https://doi.org/10.1063/1.1785131.

[25] Rozema, W., Bae, H. J., Moin, P., and Verstappen, R., "Minimum-dissipation models for large-eddy simulation," *Physics of Fluids*, Vol. 27, No. 8, 2015. https://doi.org/10.1063/1.4928700.

[26] Wang, Y., Gao, Y., and Liu, C., "Letter: Galilean invariance of Rortex," *Physics of Fluids*, Vol. 30, No. 11, 2018, p. 111701. https://doi.org/10.1063/1.5058939.

[27] You, D., Ham, F., and Moin, P., "Discrete conservation principles in large-eddy simulation with application to separation control over an airfoil," *Physics of Fluids*, Vol. 20, No. 10, 2008. https://doi.org/10.1063/1.3006077.

[28] Stüben, K., "Algebraic multigrid (AMG): experiences and comparisons," *Applied Mathematics and Computation*, Vol. 13, No. 3–4, 1983, pp. 419–451. https://doi.org/10.1016/0096-3003(83)90023-1.

[29] Yang, Q., and Wang, M., "Boundary-layer noise induced by arrays of roughness elements," *Journal of Fluid Mechanics*, Vol. 727, 2013, pp. 282–317. https://doi.org/10.1017/jfm.2013.190.

[30] Zhou, D., Wang, K., and Wang, M., "Large-eddy simulation of an axisymmetric boundary layer on a body of revolution," *AIAA Aviation 2020 Forum*, p. 2020-2989. https://doi.org/10.2514/6.2020-2989.

[31] Zhou, D., Wang, K., and Wang, M., "Computation of rotor noise generation in a thick axisymmetric turbulent boundary layer," *AIAA Aviation 2021 Forum*, p. 2021-2186. https://doi.org/10.2514/6.2021-2186.

[32] Wang, M., and Moin, P., "Dynamic wall modeling for large-eddy simulation of complex turbulent flows," *Physics of Fluids*, Vol. 14, No. 7, 2002, pp. 2043–2051. https://doi.org/10.1063/1.1476668.

[33] Johnson, P. L., "A physics-inspired alternative to spatial filtering for large-eddy simulations of turbulent flows," *Journal of Fluid Mechanics*, Vol. 934, 2022, p. A30. https://doi.org/10.1017/jfm.2021.1150.

[34] Kamal, M., and Johnson, P. L., "Artificial bottleneck effect in large eddy simulations," *Physical Review Fluids*, Vol. 9, 2024, p. 084605. https://doi.org/10.1103/PhysRevFluids.9.084605.

[35] Lee, M., and Moser, R. D., "Direct numerical simulation of turbulent channel flow up to $Re_\tau \approx 5200$," *Journal of Fluid Mechanics*, Vol. 774, 2015, pp. 395–415. https://doi.org/10.1017/jfm.2015.268.

[36] Lozano-Durán, A., and Bae, H. J., "Error scaling of large-eddy simulation in the outer region of wall-bounded turbulence," *Journal of Computational Physics*, Vol. 392, 2019, pp. 532–555. https://doi.org/10.1016/j.jcp.2019.04.063.

[37] Maeyama, H., and Kawai, S., "Near-wall numerical coherent structures and turbulence generation in wall-modelled large-eddy simulation," *Journal of Fluid Mechanics*, Vol. 969, 2023, p. A29. https://doi.org/10.1017/jfm.2023.575.

[38] Zhou, D., and Bae, H. J., "Sensitivity analysis of wall-modeled large-eddy simulation for separated turbulent flow," *Journal of Computational Physics*, Vol. 506, 2024, p. 112948. https://doi.org/10.1016/j.jcp.2024.112948.